

# Direct Cytosolic MicroRNA Detection Using Single-Layer Perfluorinated Tungsten Diselenide Nanoplatform

Yang Song,<sup>†,‡,ID</sup> Xu Yan,<sup>†,‡,ID</sup> Grayson Ostermeyer,<sup>§</sup> Suiqiong Li,<sup>†</sup> Lingbo Qu,<sup>\*,||</sup> Dan Du,<sup>†,ID</sup> Zhaohui Li,<sup>\*,||,ID</sup> and Yuehe Lin<sup>\*,†,ID</sup>

<sup>†</sup>School of Mechanical and Material Engineering, Washington State University, Pullman, Washington 99164, United States

<sup>‡</sup>State Key Laboratory on Integrated Optoelectronics, College of Electron Science and Engineering, Jilin University, Changchun 130012, China

<sup>§</sup>School of Biological Sciences, Washington State University, Pullman, Washington 99164, United States

<sup>||</sup>Henan Joint International Research Laboratory of Green Construction of Functional Molecules and Their Bioanalytical Applications, College of Chemistry and Molecular Engineering, Zhengzhou University, Zhengzhou 450001, China

## Supporting Information

**ABSTRACT:** Intracellular miRNA detection is vitally important for diagnosing severe diseases like cancer and for resolving the ensemble of gene products that orchestrate the living state of cells. Recent advances in the design, synthesis, and application of biocompatible nanomaterials as platforms for probing miRNAs have enabled widespread efforts to mobilize new compounds in biomedical research. Two-dimensional graphene-like nanomaterials exhibit desirable physical properties such as convenient quantum size and dynamic interface functionality. Because miRNAs regulate gene expression in the cytoplasm, it is imperative that nanomaterials targeting them are properly delivered. Unloading of nanomaterials into the cytosol using the cellular endocytic transport pathway is often hindered by an inability to cross the endosomal membrane. To address this challenge, we designed a strategy to deliver functionalized WSe<sub>2</sub> nanosheets (FWNs) to the cytosol using perfluorinated surface functionalization. Perfluorinated compounds are both hydrophobic and lipophobic, exhibiting excellent phase-separation tendency in both polar and nonpolar environments. FWNs are ~120 nm in diameter, feature low toxicity, and exhibit excellent stability in serum. The fluorinated nanostructure of FWNs enabled efficient cytosolic delivery from the endomembrane system. The fidelity of this approach was confirmed through intracellular delivery of two DNA probes (ssDNA-21 and ssDNA-210), which resulted in specific labeling of cytosolic miRNA and demonstrated the utility of this system for direct cytosolic biosensing.



MicroRNAs (miRNAs), groups of short endogenous noncoding RNAs, regulate gene expression by selectively hybridizing to target mRNAs, thereby blocking ribosomes from translating transcripts and terminating translation of code into polypeptides.<sup>1–3</sup> Aberrant expression of miRNAs is highly relative with a wide range of pathogenic processes, including tumor progression and metastasis.<sup>4–6</sup> Intrinsic characteristics of miRNA such as short lengths (~22 nucleotides), low abundance levels, and susceptibility to degradation pose challenges for miRNA sensing. To address the high demand for new clinical biotechnologies, development of simple, selective, and rapid platforms for sensing miRNAs is urgently needed. Significant attention from a variety of technical and applied fields has contributed to successful utilization of biocompatible nanomaterials, resulting in the development of several strategies for *in vitro* detection of miRNA.<sup>7,8</sup> The fluorescence strategy based on the Förster

resonance energy transfer (FRET) has been used for intracellular monitoring of miRNA. FRET-based imaging relies on energy transfer between a fluorophore that emits fluorescence and a quencher that suppresses the fluorescent light.<sup>9–12</sup> Some nanomaterials, including gold nanoparticles, carbon nanoparticles, graphene oxide, and organometallic frameworks, exhibit strong FRET effects.<sup>31–34</sup> These technologies have also been employed as nanoquenchers in miRNA detection. As a newly emerging class of nanomaterials, two-dimensional (2D) graphene-like nanomaterials, including WS<sub>2</sub>, MoS<sub>2</sub>, and MoTe<sub>2</sub> nanosheets (NSs), have aroused increasing interest because of their unique structures and physicochemical properties, such as high quenching efficien-

Received: May 16, 2018

Accepted: August 6, 2018

Published: August 6, 2018

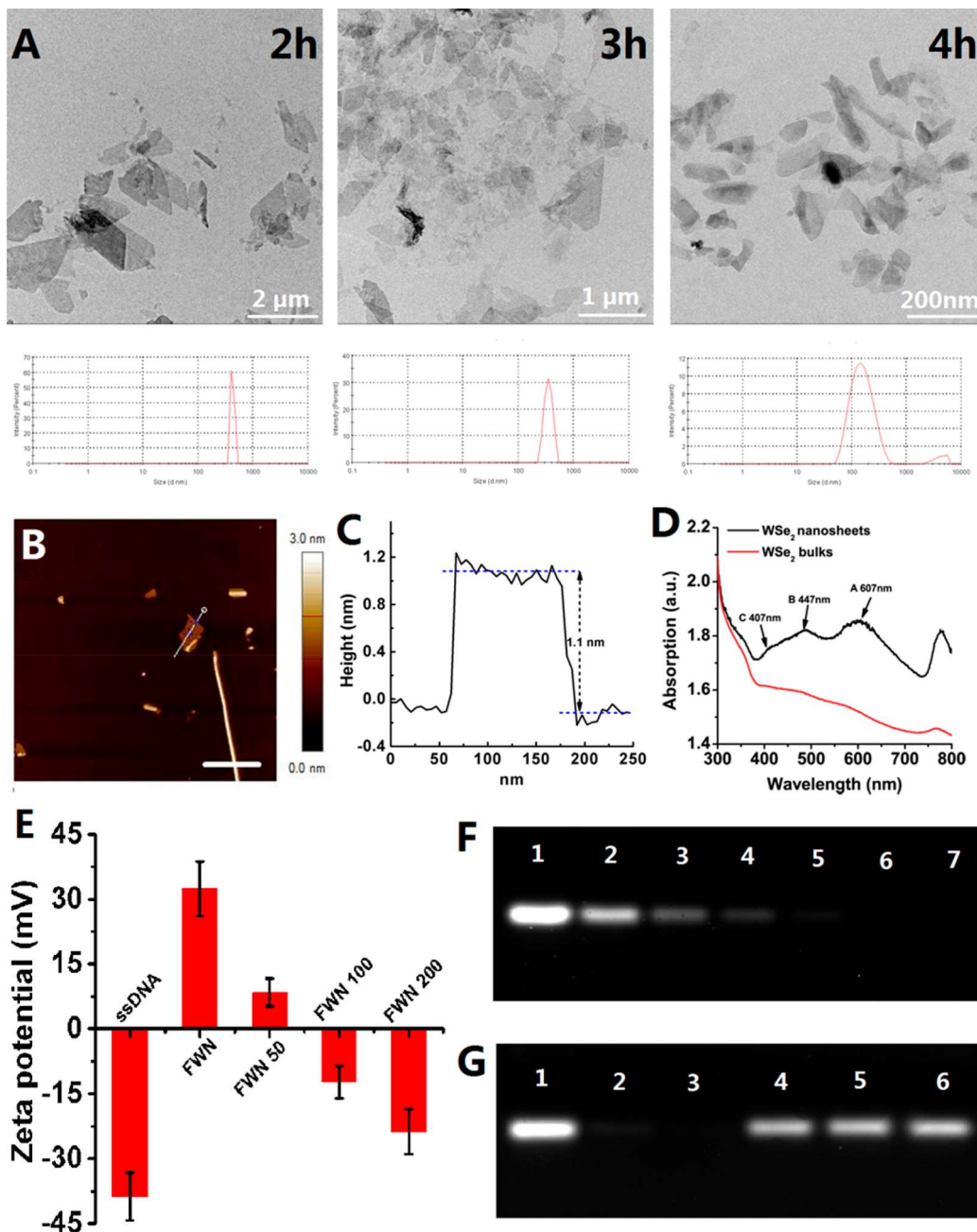


**Figure 1.** (A) TEM images of FWNs generated using variable sonication duration. The size distributions of FWNs are shown below the TEM graphs. (B) AFM image of FWNs. Scale bar: 200 nm. (C) Height profile of FWNs. Black curve in panel C represents the height profile of the section in panel B labeled with a pin. The mean height of FWNs was  $\sim 1.1$  nm. (D) UV-vis absorption of FWNs (4 h treatment) and bulk solution. (E) Change in electrokinetic potential of FWNs ( $5 \mu\text{g mL}^{-1}$ ) at  $37^\circ\text{C}$  in pH 7.4 buffer treated with various concentrations of ssDNA-21 (0, 5, 10, and 20 nM). (F) Gel retardation assay evaluating ssDNA-21 adsorption to FWNs. Lane 1: ssDNA only (10 nM); lane 2: ssDNA treated with FWN of  $0.5 \mu\text{g mL}^{-1}$ ; lane 3: ssDNA treated with FWN of  $1 \mu\text{g mL}^{-1}$ ; lane 4: ssDNA treated with FWN of  $2 \mu\text{g mL}^{-1}$ ; lane 5: ssDNA treated with FWN of  $3 \mu\text{g mL}^{-1}$ ; lane 6: ssDNA treated with FWN of  $4 \mu\text{g mL}^{-1}$ ; lane 7: ssDNA treated with FWN of  $5 \mu\text{g mL}^{-1}$ . (G) Protection of ssDNA from DNase I digestion as evaluated by electrophoresis. Lane 1: ssDNA only (10 nM); lanes 2 and 3: ssDNA (10 nM) treated with DNase I for 20 min (lane 2) and 60 min (lane 3); lane 4: ssDNA (10 nM) and FWN ( $5 \mu\text{g mL}^{-1}$ ); lanes 5 and 6: ssDNA (10 nM) and FWN ( $5 \mu\text{g mL}^{-1}$ ) treated with DNase I for 20 min (lane 5) and 60 min (lane 6).

cies, extensive material compatibilities, large surface area, and ease of functionalizing surface.<sup>8,13–18</sup> NSs have been extensively studied in drug delivery systems for controlled releasing of nutrients, drugs, and biomolecular/nucleic acid probes, which demonstrated the applications of NSs for functional biocompatibility and passive targeting.

However, one of the major obstacles that 2D NSs face in targeting and sensing intracellular gene products is the limited intracellular delivery into the cytosol. For intracellular detection, 2D NSs are taken up by cells through the endocytic pathway, which is a process that involves the physiological uptake of extracellular materials into cells by encapsulation into subcellular vesicular compartments called endosomes. Endo-

somal is a key hurdle as nanomaterial-based delivery methods traditionally result in a small fraction of entrapped vesicle (~1%) escaping into the cytoplasm.<sup>19</sup> Because miRNAs are primarily considered to regulate gene expression in the cytoplasm, loading DNA probes must be efficiently released from vesicular compartments to avoid enzymatic degradation and effectively interact with their molecular targets. Membrane-perturbing peptides and cation polymers are recent devices implemented in probe delivery systems with limited endo/lysosomal escape capability and high cytotoxicity. Few other intracellular sensing platforms that demonstrate effective endosomal release into the cytosol with minimal cytotoxicity and protection genetic molecules from digestion by nuclease are currently available.<sup>20–24</sup>

Fluorination is a widely used chemical process which introduces beneficial material properties. Addition of fluorine to a material surface can increase the therapeutic efficacy or pharmacokinetic behavior of numerous drugs by allowing the attached molecules to retain structure and function. Fluorinated compounds are both hydrophobic and lipophobic, holding a high phase-separation tendency in polar or nonpolar environments. Fluorination nanomaterials show the strong lipid bilayer affinity, which not only enhances uptake of fluorinated materials across the cell membrane but also increases the efficiency of penetrating the endosome/lysosome membranes, facilitating the endosomal escape of nanomaterials. In this study, we synthesized fluorinated tungsten diselenide NSs (FWNs) to produce an effective cytosolic miRNA detection platform. To the best of our knowledge, cytosolic delivery of 2D nanomaterials has not been demonstrated previously. In this experiment, FWN/ssDNA complexes were sequestered rapidly into the cytosol by cancer cell lines with quick endosomal escape. Molecular detection principles were described in detail in previous contributions.<sup>31–34</sup> Briefly, fluorophore-labeled ssDNA adsorbs to the surface of FWNs via electrostatic interaction and  $\pi$ – $\pi$  stacking, leading to a substantial fluorescence-quenching effect by photoinduced electron transfer (PET) from the excited band of the DNA probes-tagged fluorophore to the conduction band of FWNs. In contrast, double-stranded complexes form when ssDNA hybridizes with its target because of nucleobases being buried between negatively charged helical phosphate backbone, leading to the release of a target strand away from the surface of FWNs and retention of probe fluorescence. Intracellular miRNA-21 and miRNA-210 were successfully detected following uptake of FWNs using confocal microscopy. Effective cytosolic miRNA detection by using DNA probes loaded onto FWNs with efficient cellular uptake suggests that this nanoplatform has a great potential to be used as a new prospective nanocargo for efficient delivery and bioanalysis inside living cells.

## ■ EXPERIMENTAL SECTION

**Synthesis of WSe<sub>2</sub> NSs.** Commercial WSe<sub>2</sub> bulk was ground by a grinding miller for about 2 h. A 30 mg sample of ground WSe<sub>2</sub> powder was dispersed in 30 mL of H<sub>2</sub>SO<sub>4</sub>, and the mixture was then stirred at 37 °C for 24 h of intercalation. Then the intercalated WSe<sub>2</sub> sample was washed and centrifuged with deionized (DI) water. The intercalated WSe<sub>2</sub> sample was further ultrasonicated (150 W) for 4 h, which was centrifuged at 5000 rpm to obtain WSe<sub>2</sub> monolayer sheets.

For amine functionalization, WSe<sub>2</sub> sheets (100 mg) were initially ground by a grinding miller for about 2 h, then stirred in the solution containing SOCl<sub>2</sub> and dimethyl-formamide (DMF), and washed with dry methylene chloride to achieve the formation of WSe<sub>2</sub>–COCl. Then, the crude sample was dissolved in a mixture of sodium azide and DMF at room temperature for 48 h. The intercalated WSe<sub>2</sub> sample was further washed and centrifuged with DI water to yield WSe<sub>2</sub>–NH<sub>2</sub>. The intercalated WSe<sub>2</sub>–NH<sub>2</sub> sample was further ultrasonicated (150 W), which was centrifuged at 5000 rpm to obtain WSe<sub>2</sub>–NH<sub>2</sub> NSs.

For intercellular imaging, WSe<sub>2</sub>–NH<sub>2</sub> NSs (10 mg) and 1 mM of heptafluorobutyric anhydride/COOH-PEG-Cy5 (Mn ≈ 5000) with molar ratio of 4:1 were dissolved in 10 mL of methanol at different molar ratios. Then 100  $\mu$ L of EDC/NHS (0.1 M) in DMF was added to the solution. The mixtures were stirred for 48 h and washed with distilled water. The obtained FWNs were highly water-soluble and were stored at 4 °C for future use. For intercellular miRNA detection, WSe<sub>2</sub>–NH<sub>2</sub> NSs (10 mg) and 1 mM of heptafluorobutyric anhydride/COOH-PEG (Mn ≈ 5000) with molar ratio of 4:1 were dissolved in 10 mL of methanol at different molar ratios. Then 100  $\mu$ L of EDC/NHS (0.1 M) in DMF was added to the solution. The mixtures were stirred for 48 h and washed with distilled water.

## ■ RESULTS AND DISCUSSION

**Synthesis and Characterization of FWNs.** Single-layer WSe<sub>2</sub> nanosheets (NSs) were first prepared from commercially available WSe<sub>2</sub> using a facile one-step exfoliation method. We dispersed bulk WSe<sub>2</sub> in an intercalating agent (H<sub>2</sub>SO<sub>4</sub>) then broke the compound into NSs using the mechanical force of ultrasonication. Derived NSs were fluorinated using a process reported previously.<sup>25</sup> WSe<sub>2</sub> NSs were mixed with SOCl<sub>2</sub> in DMF solution at 4 °C to attach acyl chloride groups on the NSs. The resulting NSs were reacted with sodium azide to form aminated WSe<sub>2</sub> NSs. Subsequent reaction with perfluoro acid anhydrides at room temperature resulted in fluorinated WSe<sub>2</sub> NSs (FWNs).

The exfoliation process that broke WSe<sub>2</sub> bulk into NSs was observed using transmission electron microscopy (TEM) (Figure 1A). TEM images of FWNs after 2, 3, and 4 h of sonication treatment showed that large NSs were gradually converted into nanoscale fragments during exfoliation. After 4 h of sonication, NSs exhibited a monodisperse structure with a uniform particle size of approximately 120 nm (lower part of Figure 1A). The FWNs derived from exfoliation treatment were considered fully processed. Observation by atomic force microscopy (AFM) confirmed that FWNs possessed a single-layer morphology and a thickness of ~1.1 nm (Figure 1B,C). Optical absorption spectra for bulk and exfoliated FWN compounds are plotted in Figure 1D to highlight three key absorption signatures for FWNs. The absorption peaks located at 407, 447, and 607 nm reflect electronic transitions and coincide with expected signals for transition-metal dichalcogenides with trigonal prismatic coordination. The peaks located at 607 nm (2.043 eV) indicate the interband exciton transitions at the K point of the Brillouin zone. The two other broad peaks centered at 446 and 407 nm suggest a strong quantum size effect of FWN. FWNs exhibited narrow size distribution and positive surface charge in phosphate-buffered saline (PBS, pH ~ 7.4) (Figure 1E). Negatively charged ssDNA were expected to interact at the FWN surface by

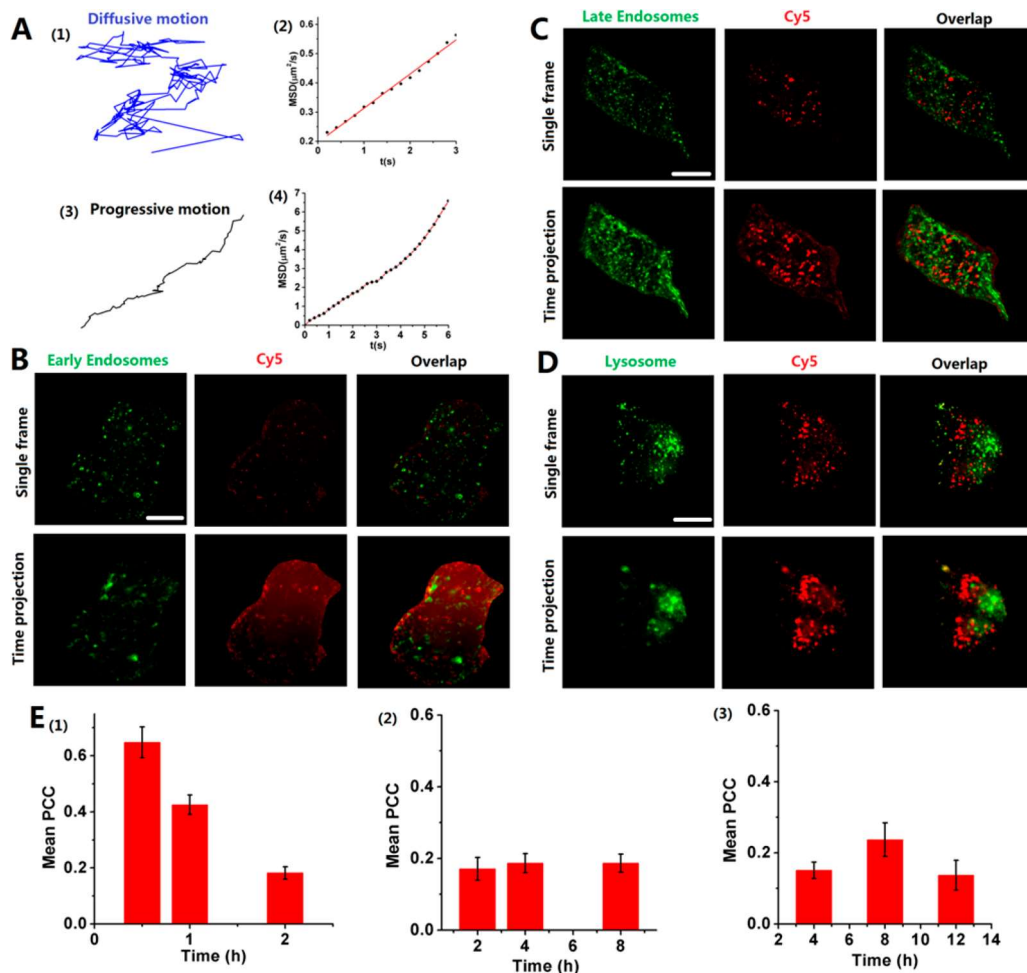


**Figure 2.** (A) (1) Diffusive tracks of FWN in cells. (2) Quantitative analysis of diffusive motion tracks. (3) Processive motility track of FWN in cells. (4) Quantitative analysis of processive motility tracks. (B) Single image (top) and time projection (bottom) of H1299 cells incubated with FWN (red) and early endosomes-GFP (green). (C) Single image (top) and time projection (bottom) of H1299 cells incubated with FWNs (red) and late endosomes-GFP (green). (D) Single image (top) and time projection (bottom) of H1299 cells incubated with FWNs (red) and lysosomes-GFP (green). (E) Mean PCC values change over time for (1) early endosomes, (2) late endosomes, and (3) lysosomes. Scale bar: 15 μm.

electrostatic interactions or π–π stacking. In the presence of ssDNA, the zeta potential of FWNs shifted from 32.4 to –23.7 mV, confirming successful adsorption of ssDNA. FWNs effectively formed complexes with ssDNA following increasing ssDNA concentrations (Figure 1F). Adsorption of ssDNA by FWNs protected ssDNA against nuclease degradation, a prerequisite for intracellular delivery of ssDNA. As shown in Figure 1G, treatment of ssDNA with DNase I (10 μU) at 20 min and 1 h resulted in complete degradation of ssDNA. Significant amounts of ssDNA in the FWN/ssDNA complex can still be detected after treatment of DNase I even at a longer incubation (1 h), indicating strong enzymatic cleavage protection of FWNs on ssDNA.

**Cytosolic Delivery of FWNs.** Potential cytotoxic attributes of FWNs were first evaluated following a standard MTT assay using H1299 human nonsmall cell lung carcinoma cells. As shown in Figure S1, almost 93% cell viability is observed after incubation with FWN for 24 h in the concentrations ranging from 1.0 to 50 μg mL<sup>-1</sup>, demonstrating the excellent biocompatibility of these FWNs. We then characterized FWN uptake using total internal reflection fluorescence (TIRF) microscopy, which allows high-resolution imaging on the cell membrane. We expected fluorescence of FWNs to

decrease in H1299 cells exponentially as the particles moved further from the optical plane in the Z direction and totally disappear 300 nm away from FWNs as we approached the ventral plasma membrane. At low concentrations (1.0 μg mL<sup>-1</sup>), FWN (labeled with PEG-Cy5, MW 5000, ratio ≈ 0.1) were efficiently delivered into living H1299 cancer cells. Internalized FWNs were motile and excluded from the nucleus (Figure S2).

We then sought to identify the endocytic pathways and cellular internalization mechanism for FWNs by measuring uptake rates under different conditions. On the basis of confocal immunofluorescence data, cellular uptake of FWN was almost stalled at 4 °C, indicating that endocytosis was energy-dependent (Figure S4a). As shown in Figure S4b, cellular uptake of FWNs was negligibly affected by the presence of chlorpromazine. FWNs exhibited some colocalization with caveolin-1 (CAV-1), flotillin-1 (FLOT-1), and cholera toxin subunit B (CTX-B) (Figure S4d–f), all resident proteins of lipid rafts. Treating H1299 cancer cells with the pharmacological inhibitor filipin, which binds cholesterol in membranes, decreased intracellular accumulation of FWNs (Figure S4c). For filipin-treated cells, FWNs only localized on the cell membrane and rarely entered the cytosol (Figure S4c).

These results suggest that endocytosis of FWNs follows the caveolae/lipid-rafts pathway.

With successful cellular internalization of the FWNs via endocytosis, we focused our investigation on the endo/lysosomal escape process. Delivery of the FWNs from the endosomal system into the cytosol was analyzed using two independent methods. The pathways of FWN diffusion in the cytosol was tracked and measured. Cytoplasm contains a highly dense network of organelles, macromolecules, and cytoskeletal elements and therefore shows a crowded environment. The cytosolic motion of particles will exhibit Brownian motion characterized by a fast diffusion coefficient. Such movement will be random and short-ranged. Endosomes coupled to molecular motors will possess long-ranged and directed motility. Thus, upon endosomal escape, FWNs transit to undirected motion. After H1299 cells were treated with FWNs, we observed both types of motility behaviors of the fluorescent FWNs in cytosol: short-ranged “hop” movement and long-ranged directional motility (Figure 2A-1,3). The experiments showed that ~80% of FWNs demonstrated the undirected movement. For FWNs demonstrating undirected hop mobility, the average  $\alpha$  (scaling exponent of MSD) was  $0.74 \pm 0.01$  and the diffusion coefficient  $D$  was  $0.103 \pm 0.006 \mu\text{m}^2 \text{s}^{-1}$  (Figure 2A-2). The diffusion coefficient of FWNs was recorded as 1.7 orders higher than that reported for endosomes.<sup>10,26</sup> These results suggest that FWNs have released from endosomes. The MSD curve of the FWNs with long-range motility was described by a quadratic function ( $R^2 = 0.99$ ), which was attributed to the molecular motor-driven motility in the microtubule (Figure 2A-4). Furthermore, the mean velocity ( $v$ ) of FWNs was  $0.317 \pm 0.008 \mu\text{m/s}$ , falling within the velocity range of intracellular endosomal motility.<sup>10,11,27–30</sup> Therefore, FWNs demonstrating long-ranged movement were still trapped inside endosomes. These results suggest that the majority of FWNs that escaped from endosomes were delivered into the cytosol.

The next set of experiments involved colocalization analysis of FWNs with endosomes and lysosomes. Colocalization of FWNs with early endosomes (EEs, marked with CellLight Early Endosomes-RFP, BacMam 2.0), late endosomes (LEs, marked with CellLight Late Endosomes-RFP, BacMam 2.0) and lysosomal compartments (marked with CellLight Lysosomes-RFP, BacMam 2.0) was investigated using confocal laser scanning microscopy (CLSM). The degree of colocalization of FWNs with these cellular vesicles was examined using time-lapse imaging, which quantified the Pearson correlation coefficient (PCC) representing the percentage of FWN fluorescence overlaid with that of RFP. The results showed that most FWNs colocalized with EEs ( $63 \pm 6\%$ ,  $N = 20$  cells) at 30 min of incubation (Figure S5). After 2 h of incubation, we found low colocalization for both EEs ( $18 \pm 3\%$ ,  $N = 20$  cells) and LEs ( $17 \pm 4\%$ ,  $N = 20$  cells), suggesting that FWNs escaped from endosomes (Figure 2E). This analysis showed that the concentration of trapped FWNs gradually decreased in EEs, while colocalization of FWNs with LEs remained at a low level for the whole observation period, indicating that the FWNs did not interact with LEs, but rather they remained in the cytosol after escape. As shown in Figure S3, before internalization, most FWNs pulsed to bond to the cell membrane demonstrated increasing fluorescent intensity over time until the cell membrane was saturated by red fluorescence. This result suggests that FWNs were undergoing uptake by cell-mediated endocytosis. FWNs bound to the cell

membrane, where they internalized into punctate structures and colocalized with EEs. Further analysis of dual color movies confirmed the release of FWNs from endosomes (Figure 2B–D). FWNs rarely colocalized with LEs and lysosomes. Although most FWNs were successfully released, ~22% were immobilized within endosomes, which may be due to the trapping in large immobile masses.

The dynamics of endosomal escape were also investigated by colocalization analysis. Figure 3A illustrates the typical escape

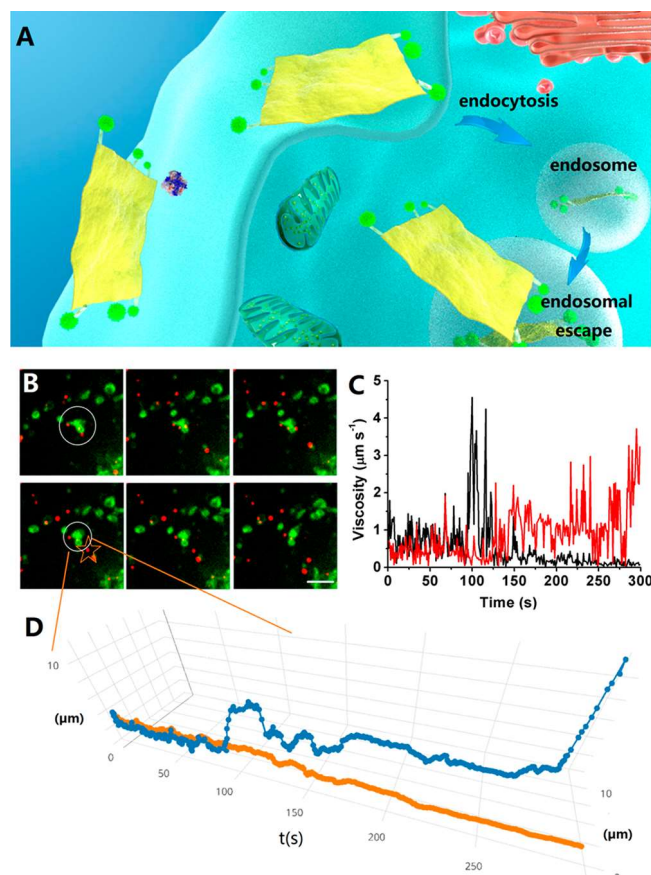


**Figure 3.** (A) Schematic illustration of FWN uptake and intracellular trafficking. (B) Selected confocal micrograph frames showing an escape event in a montage of typical FWN-labeled early endosomes (EEs) or sorting endosomes. Scale bar:  $3 \mu\text{m}$ . (C) Intracellular movement of FWNs (black) and EEs (red). (D) Plots of EE (blue) and FWN (orange) mobility as a function of time.

process of an FWN from an EE. FWNs initially follow the movement of EEs but escape endosomes and demonstrate little cross-particle (FWN) interaction thereafter. Figure 3C shows trajectories of FWNs and EEs during the escape process. Initially, FWNs and EEs followed the same trajectory because the nanoparticles were trapped within EEs. After several seconds, these two particles were separated and moved independently, indicating endosomal escape. The corresponding velocities of FWNs and EEs were significantly different after FWNs escaped (Figure 3B). Molecular motor-driven endosomes moved significantly faster than FWNs, suggesting that FWNs transitioned to diffusive motion after escape into the cytosol.

**Cytosolic miRNA Detection in Vitro.** Molecular detection principles were described in detail in a previous study. Briefly, fluorophore-labeled ssDNA adsorbs to the

surface of FWNs via electrostatic interaction and  $\pi-\pi$  stacking, leading to a substantial fluorescence-quenching effect by photoinduced electron transfer (PET) from the excited band of the DNA probes-tagged fluorophore to the conduction band of FWNs. In contrast, double-stranded complexes form when ssDNA hybridizes with its target because of nucleobases being buried between negatively charged helical phosphate backbone, leading to the release of a target strand away from the surface of FWNs and retention of probe fluorescence. The PET between FWNs and dye (Cy5) was further performed by FL lifetime measurements. The lifetime of Cy5 were obviously changed after adding FWNs. With the increasing of FWNs, the lifetime of Cy5 became shorter, indicating the effect of PET (Figure S7).

Cy5-labeled ssDNA-210 (R1), Cy3-labeled ssDNA-21 (R2), and their respective complementary targets (miRNA-210: T1 and miRNA-21: T2) were employed to investigate the detection ability of FWN, which alone lacks direct fluorescence capacity. Figure 4A shows the measured fluorescence spectra of

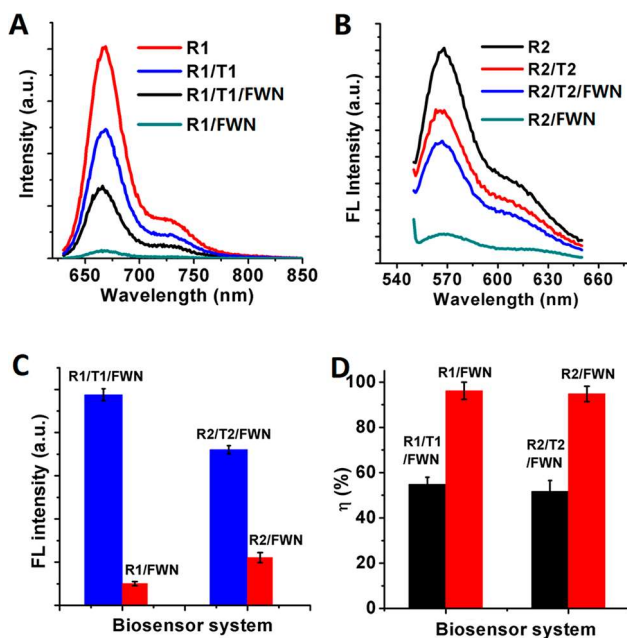


**Figure 4.** (A) Fluorescence spectra of R1 under different conditions: R1 (red curve); R1/T1 (blue curve); R1/T1/FWN (black curve); and R1/FWN (green curve). (B) Fluorescence spectra of R2 under variable treatments: R2 (black curve); R2/T2 (red curve); R2/T2/FWN (blue curve); and R2/FWN (green curve). (C) Fluorescence intensities of R1/FWN, R1/T1/FWN and R2/FWN, R2/T2/FWN. (D) Quenching efficiencies of FWNs when treated with R1, R1/T1, R2, and R2/T2.

R1 under variably bound states. Upon excitation using a 625 nm laser line, R1 exhibited a strong fluorescence emission ( $\sim 670$  nm, red curve), whereas the fluorescence intensity was quenched more than 90% after addition of FWN within 10 min, revealing a strong fluorescence-quenching ability by FWN (green curve). Fluorescence intensity of R1 was quenched more than 95% after addition of FWNs at optimal concentration ( $5 \mu\text{g mL}^{-1}$ ) within 30 min (Figure S6). FWN/R1 complexes were incubated with T1 at  $37^\circ\text{C}$  for 30 min. After hybridization with T1, R1/T1 complexes were released from the surface of FWNs, resulting in restoration of fluorescence signals (black curve). Fluorescence intensity of

R1/T1 composite was 10-fold higher than FWN/R1. After addition of FWNs, fluorescence intensity of ssDNA-21 (R2) at 570 nm (Cy3) was significantly quenched (green curve), while that of R2/T2 hybridized composite was largely retained compared to that of R1 in the presence of FWNs (blue curve) (Figure 4B). The fluorescence change for R2 (20 nM) induced by FWNs with various concentrations is shown in Figure S6. Figure 4C shows the fluorescence change for R1, R1/T1 composite, R2, and R2/T2 composite each induced by FWNs with optimal NS concentrations. The quenching efficiencies for R1 and R2 induced by FWNs under optimal concentrations are 96% and 93%, respectively, while 58% and 54% are achieved for R1/T1 and R2/T2 hybridized composites, respectively (Figure 4D). These results establish an empirical capacity for FWNs to quench fluorescence and interact compatibly with diverse DNA probe constructs.

The high fluorescence-quenching efficiency and intensity retention ability from hybridized composites suggest that FWNs may be effective for multiplex quantitative detection of miRNA. FWN/ssDNA were simultaneously incubated with various concentrations of T1 and T2 at  $37^\circ\text{C}$  for 30 min. After hybridization, R1/T1 and R2/T2 complexes were released from FWNs, restoring fluorescence. As shown in Figure 5, the

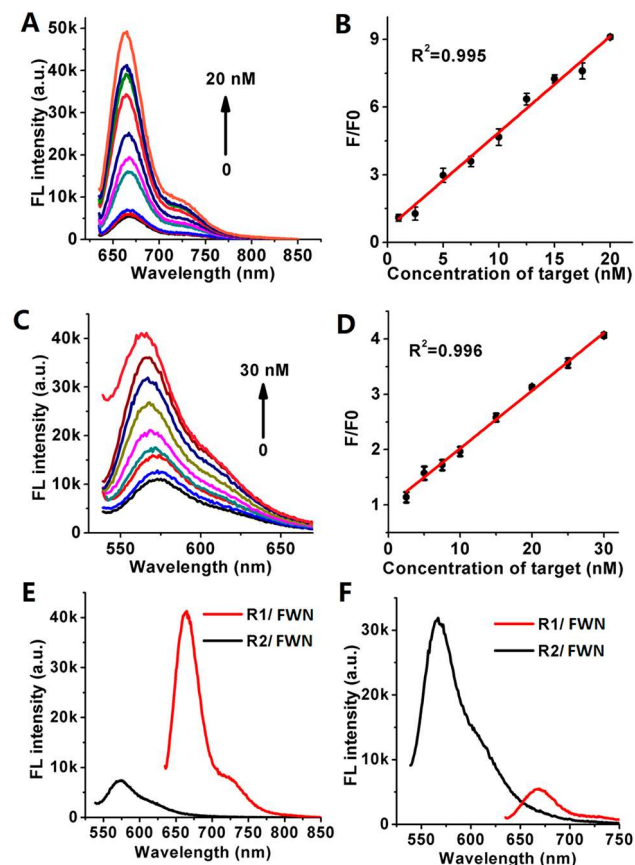


**Figure 5.** (A) Fluorescence spectra of R1/R2/FWN in the presence of different concentrations of T1. (B) Calibration curve for miRNA detection in panel A. (C) Fluorescence spectra of R1/R2/FWN in the presence of different concentrations of T2. (D) Calibration curve for miRNA detection in panel C. Sensitivity analysis of the FWN/ssDNA probe based on differential affinity toward T1 and T2. Two probes (R1: 10 nM and R2: 20 nM) were incubated with FWNs and detected in the presence of different targets (T1: red curve, 10 nM in panel E; T2: black curve, 20 nM in panel F).

FWN/ssDNA complex responds to specific target T1 or T2. In the presence of T1, we observed the specific emission from R1 at 660 nm (Figure 5E). Similarly, the presence of T2 will lead to the emission of R2 at 570 nm (Figure 5F). These results imply that this nanoprobe exhibited excellent selectivity for specific target miRNA. FWN/ssDNA were simultaneously incubated with various concentrations of T1 or T2. As displayed in Figure 5A, fluorescence intensity increases relative to T1 concentration and exhibits a linear relationship over the range of 0–20 nM with a detection limit of 0.75 nM (Figure 5B). Note that the fluorescence did not fully recover to that of R1, which is due to the interaction between R1/T1 and FWNs, which resulted in negligible adsorption of R1/T1 on FWNs. The percentage of R2 hybridized with T2 to form a composite increased with increasing T2 concentration, resulting in more R2 fluorescence retention (Figure 5C). This sensing system shows a linear range between 0 and 30 nM for T2 with a detection limit of 1.0 nM (Figure 5D). The results are close to that of a previously reported MoS<sub>2</sub>-based DNA assay and indicate that the system is more effective than other nanomaterial-based probes (Table S2).

Selective recognition capability is a very significant character to investigate the performance of the FL sensing platform, especially for platforms with potential applications in intracellular detection and imaging. The selectivity of this assay has been studied. As shown in Figure S10, after hybridization with miRNA21 and miRNA 210, ssDNA/miRNA21 or ssDNA/miRNA 210 complexes were released from the surface of FWNs, resulting in restoration of fluorescence signals. However, after addition of miRNA155, no obvious fluorescence intensity restoration was observed at 570 nm (Cy3) or 670 nm (Cy5). Besides, as shown in Figure S11, after hybridization with miRNA21 and miRNA 210 at the same time, these nanoprobes can get restoration of fluorescence signals at both 570 nm (Cy3) and 670 nm (Cy5), indicating these nanoprobes can detect two kinds of miRNAs simultaneously. In addition, to assess the specificity of the nanoprobes for the detection of miRNA, the influence of some common substance including amino acids, glucose, and proteins was studied in aqueous solutions. As shown in Figure S9, after the addition of the above substances, the FL intensity of the FWN/ssDNA system remained nearly constant, and only after the addition of miRNA210 or miRNA 21 did the FL intensity show obvious recovery. The results indicated that the sensing platform showed the high selectivity to miRNA 210 or miRNA21.

Stability is also a very significant character to investigate the performance of the FL sensing platform, especially for platforms with potential applications in intracellular detection and imaging. Therefore, to assess the stability of the nanoprobes, the influence of some common substance including amino acids, glucose, and proteins was studied in aqueous solutions. As shown in Figure S8, after the addition of the above substances, the FL intensity of the nanoprobes system remained nearly constant (FL intensity change less than 1%), which indicated that the sensing platform showed good stability. In addition, the DLS and zeta potential was studied. As shown in Figure S12, the DLS and zeta potential of nanoprobes show negligible change even after one month of storage. This indicates the good stability of the nanoprobes.

To investigate the capability of FWN/ssDNA for cytosolic miRNA detection in cancer cells, we introduced our sensing system in H1299 cancer cells and analyzed the results using confocal microscopy. As shown in Figure 6, H1299 cells

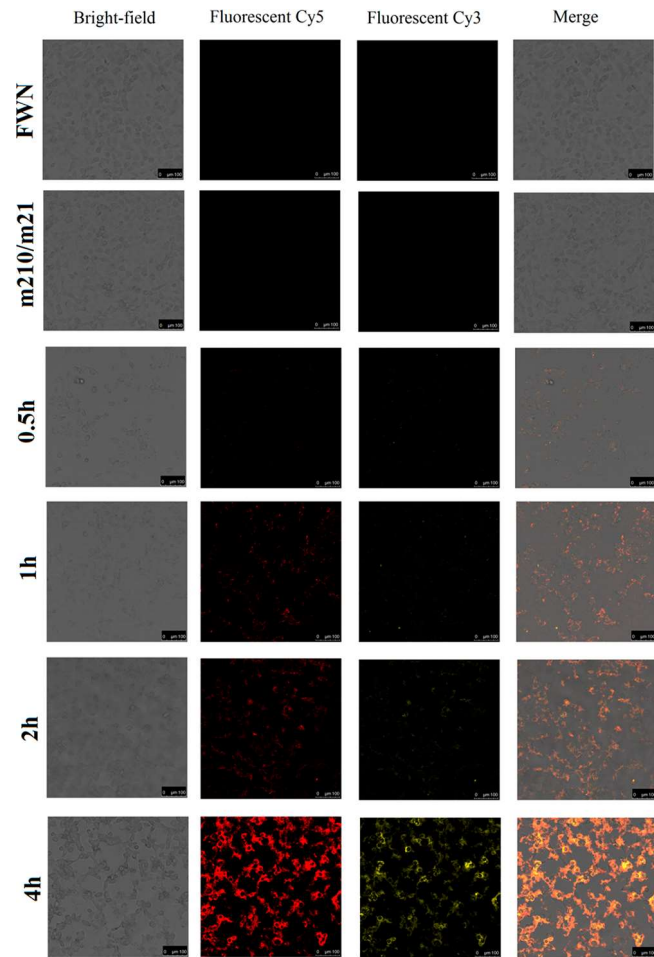


**Figure 6.** Simultaneous confocal microscopy images of multiple miRNAs in H1299 cells treated with a FWN/ssDNA probe with various incubation times (0.5–4 h). The left-most column images are bright-field micrographs; the left-center images are Cy5 fluorescence micrographs associated with miRNA-210; the right-center images are Cy3 fluorescence micrographs associated with miRNA-21; the right-most images are overlays of fluorescence and bright-field images. Scale bars: 100  $\mu$ m.

exhibits bright red and yellow fluorescence signals with the fluorescence signal-off probe. Fluorescence intensity increases with ssDNA probe incubation time and reaches a maximum value at 4 h. A flow cytometer was used to measure the fluorescence signals (Figure S13). When H1299 cells were incubated with pure FWNs, no fluorescence intensity was observed. When H1299 cells were incubated with FWN/R2, Cy3 fluorescence increased ~6.7-fold at 1 h and ~32.8-fold at 4 h. When cells were incubated with FWN/R1, Cy5 fluorescence increased ~7.0-fold at 1 h and ~27.3-fold at 4 h. With FWN/R1/R2 incubation, ~8.1-fold and ~6.1-fold increases about Cy3 and Cy5 fluorescence intensity were observed after 1 h, and ~31.1-fold and ~26.7-fold increases can still be observed 4 h post-transfection. Compared to cells separately treated with FWN/R1 and FWN/R2, similar fluorescence response was observed because of less interference between R1 and R2. FWN/ssDNA can also recognize other miRNA-210-positive and miRNA-21-positive cells, as observed by the red and yellow fluorescence signals detected in A549 adenocarcinoma human alveolar basal epithelial cells (Figure S14). In parallel experiments, we also treated the

bEnd.3 cells (miRNA-210-negative and miRNA-21-negative cells) with FWN/ssDNA. When the nanoprobe was further added to bEnd.3 cells, no luminescence intensity was observed (**Figure S15**). To verify that fluorescent signals from FWN/ssDNA probes originated from the cytosol but not the endosome/lysosome system, we conjugated R1 and R2 on WSe<sub>2</sub>-PEG NSs. We treated H1299 cells with WSe<sub>2</sub>/ssDNA and measured greatly reduced Cy3 and Cy5 fluorescence at 4 h of incubation as compared to FWN/ssDNA (**Figure S16**). These results demonstrated that the FWN/ssDNA probe could be used to detect multiple miRNAs in the cytoplasm.

## CONCLUSION

In summary, we have successfully indicated that fluorinated tungsten diselenide NSs have a high fluorescence-quenching ability and demonstrate differential affinity for probe DNA, which enable them to serve as selective and sensitive platforms for miRNA detection. These experiments provided evidence for competent uptake of FWNs by the cellular endosomal transport pathway and biocompatibility within cytoplasm after being released from early endosomes. Therefore, we believe that this simple sensing platform provides a novel approach for multiplexed detection of biological molecules.

## ASSOCIATED CONTENT

### Supporting Information

The Supporting Information is available free of charge on the ACS Publications website at DOI: [10.1021/acs.analchem.8b02193](https://doi.org/10.1021/acs.analchem.8b02193).

Cytotoxicity of FWNs for H1299 cells, statistical analysis and reproducibility investigation, live cell imaging and single-particle tracking, fluorescent miRNA detection, cell viability of H1299 cells after incubating with different concentrations of FWNs, and lipid raft/caveolae-mediated endocytosis ([PDF](#))

## AUTHOR INFORMATION

### Corresponding Authors

\*E-mail: [yuehe.lin@wsu.edu](mailto:yuehe.lin@wsu.edu).

\*E-mail: [zhaohui.li@zzu.edu.cn](mailto:zhaohui.li@zzu.edu.cn).

\*E-mail: [qulingbo@zzu.edu.cn](mailto:qulingbo@zzu.edu.cn).

### ORCID

Yang Song: [0000-0003-0848-4831](https://orcid.org/0000-0003-0848-4831)

Xu Yan: [0000-0003-2152-675X](https://orcid.org/0000-0003-2152-675X)

Dan Du: [0000-0003-1952-4042](https://orcid.org/0000-0003-1952-4042)

Zhaohui Li: [0000-0003-3946-0656](https://orcid.org/0000-0003-3946-0656)

Yuehe Lin: [0000-0003-3791-7587](https://orcid.org/0000-0003-3791-7587)

### Author Contributions

<sup>†</sup>Y.S. and X.Y. equally contributed to this work.

### Notes

The authors declare no competing financial interest.

## ACKNOWLEDGMENTS

This work was supported by Washington State University start up fund. Y.L. thanks the National Natural Science Foundation of China for financial support (81000976).

## REFERENCES

- Filipowicz, W.; Bhattacharyya, S. N.; Sonenberg, N. *Nat. Rev. Genet.* **2008**, *9*, 102–114.
- Dong, H.; Meng, X.; Dai, W.; Cao, Y.; Lu, H.; Zhou, S.; Zhang, X. *Anal. Chem.* **2015**, *87*, 4334–4340.
- Lu, W.; Chen, Y.; Liu, Z.; Tang, W.; Feng, Q.; Sun, J.; Jiang, X. *ACS Nano* **2016**, *10*, 6685–6692.
- Liu, X.; Aizen, R.; Freeman, R.; Yehezkel, O.; Willner, I. *ACS Nano* **2012**, *6*, 3553–3563.
- Zhao, Z.; Fan, H.; Zhou, G.; Bai, H.; Liang, H.; Wang, R.; Zhang, X.; Tan, W. *J. Am. Chem. Soc.* **2014**, *136*, 11220–11223.
- Debouck, C.; Goodfellow, P. N. *Nat. Genet.* **1999**, *21*, 48–50.
- Zhang, Y.; Zheng, B.; Zhu, C.; Zhang, X.; Tan, C.; Li, H.; Chen, B.; Yang, J.; Chen, J.; Huang, Y.; Wang, L.; Zhang, H. *Adv. Mater.* **2015**, *27*, 935–939.
- Yuan, Y.; Li, R.; Liu, Z. *Anal. Chem.* **2014**, *86*, 3610–3615.
- Zhang, X.; Xiao, Y.; Qian, X. *Angew. Chem., Int. Ed.* **2008**, *47*, 8025–8029.
- Li, X.; Gao, X.; Shi, W.; Ma, H. *Chem. Rev.* **2014**, *114*, 590–659.
- Chan, J.; Dodani, S. C.; Chang, C. *Nat. Chem.* **2012**, *4*, 973–984.
- Mizukami, S.; Watanabe, S.; Hori, Y.; Kikuchi, K. *J. Am. Chem. Soc.* **2009**, *131*, 5016–5017.
- Zhu, C.; Zeng, Z.; Li, H.; Li, F.; Fan, C.; Zhang, H. *J. Am. Chem. Soc.* **2013**, *135*, 5998–6001.
- Xi, Q.; Zhou, D.-M.; Kan, Y.-Y.; Ge, J.; Wu, Z.-K.; Yu, R.-Q.; Jiang, J.-H. *Anal. Chem.* **2014**, *86*, 1361–1365.
- Ramakrishna Matte, H. S. S.; Gomathi, A.; Manna, A. K.; Late, D. J.; Datta, R.; Pati, S. K.; Rao, C. N. R. *Angew. Chem.* **2010**, *122*, 4153–4156.
- Ge, J.; Tang, L.-J.; Xi, Q.; Li, X.-P.; Yu, R.-Q.; Jiang, J.-H.; Chu, X. *Nanoscale* **2014**, *6*, 6866–6872.
- Hwang, H.; Kim, H.; Cho, J. *Nano Lett.* **2011**, *11*, 4826–4830.
- Sen, U. K.; Mitra, S. *ACS Appl. Mater. Interfaces* **2013**, *5*, 1240–1247.
- Stewart, M. P.; Sharei, A.; Ding, X.; Sahay, G.; Langer, R.; Jensen, K. F. *Nature* **2016**, *538*, 183.
- Dowdy, S. F. *Nat. Biotechnol.* **2017**, *35*, 222.
- Verma, A.; Uzun, O.; Hu, Y.; Hu, Y.; Han, H.-S.; Watson, N.; Chen, S.; Irvine, D. J.; Stellacci, F. *Nat. Mater.* **2008**, *7*, 588.
- Yu, C.; Qian, L.; Ge, J.; Fu, J.; Yuan, P.; Yao, S. C. L.; Yao, S. Q. *Angew. Chem., Int. Ed.* **2016**, *55*, 9272–9276.
- Wang, P.; Zhang, L.; Zheng, W.; Cong, L.; Guo, Z.; Xie, Y.; Wang, L.; Tang, R.; Feng, Q.; Hamada, Y.; Gonda, K.; Hu, Z.; Wu, X.; Jiang, X. *Angew. Chem., Int. Ed.* **2018**, *57*, 1491–1496.
- Jiang, Y.; Tang, R.; Duncan, B.; Jiang, Z.; Yan, B.; Mout, R.; Rotello, V. M. *Angew. Chem., Int. Ed.* **2015**, *54*, 506–510.
- Wang, M.; Liu, H.; Li, L.; Cheng, Y. *Nat. Commun.* **2014**, *5*, 3053.
- Derivery, E.; Seum, C.; Daeden, A.; Loubéry, S.; Holtzer, L.; Jülicher, F.; Gonzalez-Gaitan, M. *Nature* **2015**, *528*, 280.
- Soppina, V.; Rai, A. K.; Ramaiya, A. J.; Barak, P.; Mallik, R. *Proc. Natl. Acad. Sci. U. S. A.* **2009**, *106*, 19381–19386.
- Pfeffer, S. R. *Nat. Cell Biol.* **1999**, *1*, E145.
- Bielska, E.; Higuchi, Y.; Schuster, M.; Steinberg, N.; Kilaru, S.; Talbot, N. J.; Steinberg, G. *Nat. Commun.* **2014**, *5*, S097.
- Bhatia, D.; Arumugam, S.; Nasilowski, M.; Joshi, H.; Wunder, C.; Chambon, V.; Prakash, V.; Grazon, C.; Nadal, B.; Maiti, P. K.; Johannès, L.; Dubertret, B.; Krishnan, Y. *Nat. Nanotechnol.* **2016**, *11*, 1112–1119.
- Yang, Y. J.; Huang, J.; Yang, X. H.; Quan, K.; Wang, H.; Ying, L.; Xie, N. L.; Ou, M.; Wang, K. M. *J. Am. Chem. Soc.* **2015**, *137*, 8340–8343.
- Wang, Y. H.; Bao, L.; Liu, Z. H.; Pang, D. W. *Anal. Chem.* **2011**, *83*, 8130–8137.
- Wang, Y.; Li, Z. H.; Hu, D. H.; Lin, C. T.; Li, J. H.; Lin, Y. H. *J. Am. Chem. Soc.* **2010**, *132*, 9274–9276.
- Ma, Y. X.; Wang, S. G.; Wang, L. Y. *TrAC, Trends Anal. Chem.* **2015**, *65*, 13–21.